

Dynamical effects as a window into van der Waals interactions in grazing-incidence fast He-atom diffraction from KCl(001)

G. A. Bocan^{1,*}, H. Breiss², S. Szilasi², A. Momeni^{2,3}, E. M. Staicu Casagrande², E. A. Sánchez^{1,4},
M. S. Gravielle^{5,†} and H. Khemliche²

¹*Instituto de Nanociencia y Nanotecnología - Nodo Bariloche (CNEA-CONICET), Centro Atómico Bariloche, Av. Bustillo 9500, 8400 S.C. de Bariloche, Argentina*

²*Université Paris-Saclay, CNRS, Institut des Sciences Moléculaires d'Orsay, 91405 Orsay, France*

³*CY Cergy Paris Université, F-95000 Cergy, France*

⁴*Instituto Balseiro (U. N. Cuyo), Centro Atómico Bariloche, Av. Bustillo 9500, 8400 S.C. de Bariloche, Argentina*

⁵*Instituto de Astronomía y Física del Espacio (UBA-CONICET), Casilla de Correo 67, Sucursal 28, C1428EGA Buenos Aires, Argentina*



(Received 14 October 2021; accepted 18 November 2021; published 1 December 2021)

In this paper we address, both experimentally and theoretically, the very grazing scattering of He atoms off KCl(001) with incidence along the $\langle 100 \rangle$ channel. Our theoretical model combines a semiquantum description of the scattering dynamics and a high-precision interaction potential. By means of a thorough analysis of the quantum phase for in-plane scattering and rainbow trajectories, we are able to connect the presence of the physisorption well with the significant enhancements of the corrugation and rainbow angle, relative to the hard corrugated wall predictions. We trace this connection to dynamical effects on the incident and scattered beams due to their traversing of the physisorption well. Finally, we show that the inclusion of van der Waals interactions in the potential improves the theoretical accord with experiments for both the corrugation and the rainbow angle.

DOI: [10.1103/PhysRevB.104.235401](https://doi.org/10.1103/PhysRevB.104.235401)

I. INTRODUCTION

Physisorption wells are a well-known feature of He-surface systems [1], traditionally attributed to polarization and vdW attractive terms in the potential. Despite their typical shallowness (depth ~ 10 meV), a recent study of grazing-incidence fast atom diffraction (GIFAD) for the He-KCl(001) system showed that this potential feature results in a sharp increase of the surface corrugation and rainbow angle for incidence along the $\langle 110 \rangle$ channel with very low normal energy ($E_{\perp} < 60$ meV) [2]. The key factor enabling this unexpected connection, besides GIFAD's high sensitivity to details of the surface electronic density, was the soft character of the He-surface interaction, i.e., dynamical effects.

An additional appealing aspect of physisorption wells is their location at He-surface distances where both polarization and van der Waals (vdW) interactions are expected to significantly contribute to the potential, a fact that has been mentioned in recent GIFAD studies for He-LiF(001) [3], Ne-LiF(001) [4], and He-KCl(001) [2]. However, all three cases focused on the $\langle 110 \rangle$ incidence channel, where the leading order dispersive force is likely given by polarization [5], which may hide vdW contributions. In fact, in Ref. [2], calculations performed with a density functional theory (DFT) potential in which the Perdew-Burke-Ernzenhof (PBE) [6] exchange-correlation functional implicitly includes polarization but neglects vdW contributions, quantitatively captured

the experimental corrugation and rainbow features, while alternative functionals that included vdW yielded no significant improvement on the theory-experiment accord.

In this context, in the present paper we address the very grazing (low normal energy $E_{\perp} = E \sin^2 \theta_i$ with E the impact energy and θ_i the glancing incidence angle) scattering of He atoms off KCl(001) with incidence along the $\langle 100 \rangle$ channel. We perform a thorough analysis of the role dynamical effects play as probes of the physisorption well. The relevant physical quantities for this study are the surface corrugation and the rainbow angle, given their already reported sensitivity to dynamical effects which, for normal energies $E_{\perp} < 60$ meV, are particularly enhanced by the attractive potential [2].

Concerning vdW interactions, heretofore they have proven rather elusive for GIFAD [2,4,7–11]. In this regard, the considered grazing incidence atom-surface scattering problem presents a combination of very favorable conditions for their exploration: (i) a polarization-free incidence channel, (ii) scattering conditions which keep He-surface distances large enough for vdW to be relevant, (iii) significant changes in the physisorption region when potentials that include vdW interactions are used instead of the reference PBE one, and (iv) dynamical effects which, for very low normal energies, turn the surface corrugation and rainbow angle sensitive to subtle changes in the physisorption region.

The pillars supporting our analysis are a DFT-based high precision potential built without incorporating experimental information of any sort, the surface initial value representation (SIVR) [12,13] which is a semiquantum approach to describe the scattering dynamics and GIFAD experimental patterns for $E_{\perp} < 200$ meV. Additional literature regarding

*Corresponding author: gisela.bocan@cab.cnea.gov.ar

†Corresponding author: msilvia@iafe.uba.ar

GIFAD studies of the He-KCl(001) system can be found in Refs. [2,9,14–17].

This paper is organized as follows: In Secs. II and III, we briefly summarize the experimental method and theoretical model; in Sec. IV A we present and discuss experimental and simulated diffraction charts for the reference PBE potential; in Sec. IV B, we analyze the potential energy surfaces (PESs) obtained from different vdW approaches; in Sec. IV C, we investigate dynamical contributions to the surface corrugation, as well as to the quantum phase; in Sec. IV D, we focus on the dynamical effects on the rainbow angle; in Sec. IV E, we address vdW contributions to the surface corrugation and the rainbow angle; and in Sec. V, we review our main results and outline our conclusions.

II. EXPERIMENTAL METHOD

The experiments were performed in a setup already described in Refs. [2,18]. A brief outline of the procedure follows. The KCl(001) sample was cleaved in air and immediately introduced into the ultrahigh-vacuum chamber to be mounted on a five-axis manipulator. It was prepared by annealing at about 650 K and its cleanness and crystallographic order were verified from the resulting well-defined GIFAD patterns. The $^4\text{He}^0$ beam was obtained by the neutralization of a He^+ beam (with 300 to 600 eV primary energies) and subsequent collimation to a beam divergence lower than 1 mrad by a set of apertures of $0.4 \times 0.09 \text{ mm}^2$ placed 0.36 m apart. The two-dimensional angular distributions of scattered projectiles were collected by a detector formed by microchannel plates, a phosphor-coated screen and a CCD camera placed in the forward direction at a distance of 1.27 m. From the recorded GIFAD patterns, the effective surface corrugation and rainbow angle were derived as explained in detail in Refs. [2,19] (particularly, see Supplemental Material of Ref. [2]).

III. THEORETICAL MODEL

The simulations of the scattering process yielding the GIFAD patterns were performed by means of the SIVR method combined with high-precision DFT-based PESs for the He-KCl(001) system. Following, we give a brief description of both of these ingredients.

A. SIVR approach

The SIVR method is a semiclassical model for grazing atom-surface scattering that takes into account quantum effects, such as interferences, coherence lengths, and classically forbidden transitions, without losing the appealing and easily understandable description in terms of classical scattering trajectories. The SIVR approximation is based on the well-known IVR approach [20] which, within a Feynman path integral formulation of quantum mechanics, introduces Van Vleck's approximation [21] for the quantum time-evolution operator, without the additional stationary phase approximation, of customary use in semiclassical methods. The IVR method provides results in excellent agreement with the full quantum values for a wide variety of atomic, molecular and nuclear processes [20,22–27], which demonstrates its ability

to describe quantum effects in complex systems evolving over time.

Within the SIVR model, the IVR time-evolution operator acts on the initial unperturbed state of the impinging projectile, giving rise to the SIVR scattering state as a function of the time t , $|\Psi^{(\text{SIVR})}(t)\rangle$, with outgoing asymptotic conditions. This scattering state can be expressed in terms of an ensemble of classical trajectories with different initial conditions, where the correlation among nearby trajectories is introduced by a determinant associated with the Maslov function. Within the quantum time-dependent distorted-wave formalism [28], $|\Psi^{(\text{SIVR})}(t)\rangle$ is used to produce the SIVR transition amplitude $A^{(\text{SIVR})}$ that reads

$$A^{(\text{SIVR})} = \int d\mathbf{r}_o f_s(\mathbf{r}_o) \int d\mathbf{k}_o f_m(\mathbf{k}_o) a^{(\text{SIVR})}(\mathbf{r}_o, \mathbf{k}_o), \quad (1)$$

where $a^{(\text{SIVR})}(\mathbf{r}_o, \mathbf{k}_o)$ is the partial transition amplitude associated with the classical projectile path $\mathbf{r}_t \equiv \mathbf{r}_t(\mathbf{r}_o, \mathbf{k}_o)$, with \mathbf{r}_o and \mathbf{k}_o , respectively, being the starting (at $t = 0$) position and momentum. The corresponding functions $f_s(\mathbf{r}_o)$ and $f_m(\mathbf{k}_o)$ describe the spatial and momentum profiles of the initial coherent wave packet at a fixed distance Z_0 from the surface where the time evolution is started.

From Eq. (1), it is clear that the transition amplitude $A^{(\text{SIVR})}$ contains the interference among different partial amplitudes $a^{(\text{SIVR})}$ associated with a given incident wave packet, which is the ultimate origin of quantum effects. Therefore, the diffraction is mainly governed by the t evolution of the phase of $a^{(\text{SIVR})}(\mathbf{r}_o, \mathbf{k}_o)$, which is given, except for the Maslov phase (i.e., an integer number times $\pi/2$), by

$$\Phi_t^{(\text{SIVR})} = \phi_t^{(\text{SIVR})} - \mathbf{Q} \cdot \mathbf{r}_o, \quad (2)$$

where $\mathbf{Q} = \mathbf{K}_f - \mathbf{K}_i$ is the projectile momentum transfer, with \mathbf{K}_f (\mathbf{K}_i) the final (initial) projectile momentum, and

$$\phi_t^{(\text{SIVR})} = \int_0^t dt' \left[\frac{1}{2m_P} (\mathbf{K}_f - \mathbf{p}_{t'})^2 - V_{\text{PS}}(\mathbf{r}_{t'}) \right], \quad (3)$$

with $\mathbf{p}_t = m_P d\mathbf{r}_t/dt$ being the classical projectile momentum, m_P the projectile mass, and $V_{\text{PS}}(\mathbf{r}_t)$ the projectile-surface interaction along the trajectory. For more details of the SIVR model, we refer the reader to Refs. [12,13].

B. Potential energy surface

To build the PES we considered a relaxed KCl(001) surface and a three-dimensional (3D) grid of positions \mathbf{R}_i for the He atom. By means of DFT, as implemented in the QUANTUM ESPRESSO package [29], we calculated the potential energy for each of these configurations. From the resulting energy grid the projectile-surface potential of an arbitrary configuration $V_{\text{PS}}(\mathbf{R})$ can be evaluated using the corrugation reducing procedure [30] and a 3D cubic spline interpolation. We performed the DFT calculations with the PBE exchange-correlation functional [6], which leaves vdW interactions out. We built three additional PESs, labeled vdW1, vdW2, and vdW3, which include vdW interactions, respectively using the rVV10 [31], DF2b86r [32], and D2 [33] approaches. Further details regarding the four PESs can be found in Refs. [2,17,34].

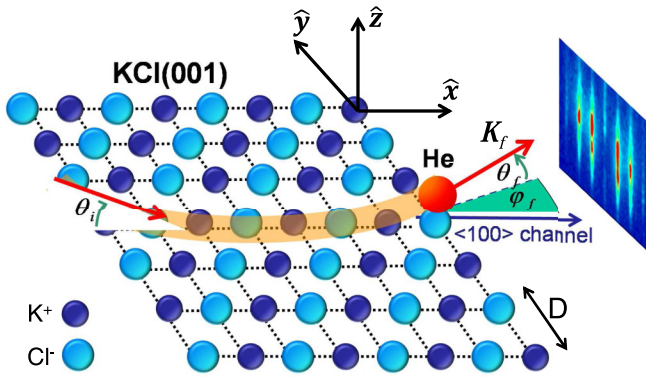


FIG. 1. Sketch of the GIFAD geometry and sample pattern. He-KCl(001) system and incidence along $\langle 100 \rangle$.

IV. RESULTS AND DISCUSSION

In this section, we present our experimental and simulated GIFAD charts for ${}^4\text{He} \rightarrow \langle 100 \rangle \text{KCl}(001)$ to then focus on the surface corrugation and the rainbow angle, both of them being GIFAD-related properties. By means of a detailed analysis of the potential features and SIVR GIFAD simulations, we expose the different effects and interactions that contribute to these properties when derived from the processing of experimental GIFAD patterns in the 5–200 meV normal energy range. Simulations have been carried out for an impact energy $E = K_i^2/(2m_p) = 600$ eV, within the validity range of the semiquantum SIVR method and corresponding to the highest value used in the experiments. Regarding SIVR, note that the key assumption of this theoretical model is the use of the IVR time-evolution operator [20], whose range of validity extends beyond the limits of most semiclassical theories [22,35–37].

The fact that experimental and theoretical results are obtained independently, i.e., without incorporating information of one another to ensure and/or optimize their mutual accord, is central to the analysis here reported. The geometry of GIFAD for ${}^4\text{He} \rightarrow \langle 100 \rangle \text{KCl}(001)$ is depicted in Fig. 1 together with relevant angles and crystallographic parameters. Note that the scattering process is depicted with a broad line to represent the entanglement of classical trajectories of similar initial conditions, discussed in Sec. III A.

A. Diffraction charts

Recent articles [2,9,17] for the He-KCl(001) system show that the overall features of the experimental GIFAD patterns are reasonably well described by means of the PBE PES. Hence, in this paper, we use this potential as a reference to study dynamical effects as well as the role of vdW interactions in the physical quantities of interest.

In Fig. 2, we depict the experimental and theoretical diffraction charts, in terms of the normal energy E_{\perp} and the final azimuthal angle φ_f . The experimental chart was built from azimuthally projected patterns for different normal energies, normalized to their respective total intensities. An analogous procedure was used for the simulated chart, obtained from the SIVR approach with the PBE PES (henceforth PBE-SIVR).

The azimuthal positions of the bright streaks are determined by the Bragg (interchannel) interference among

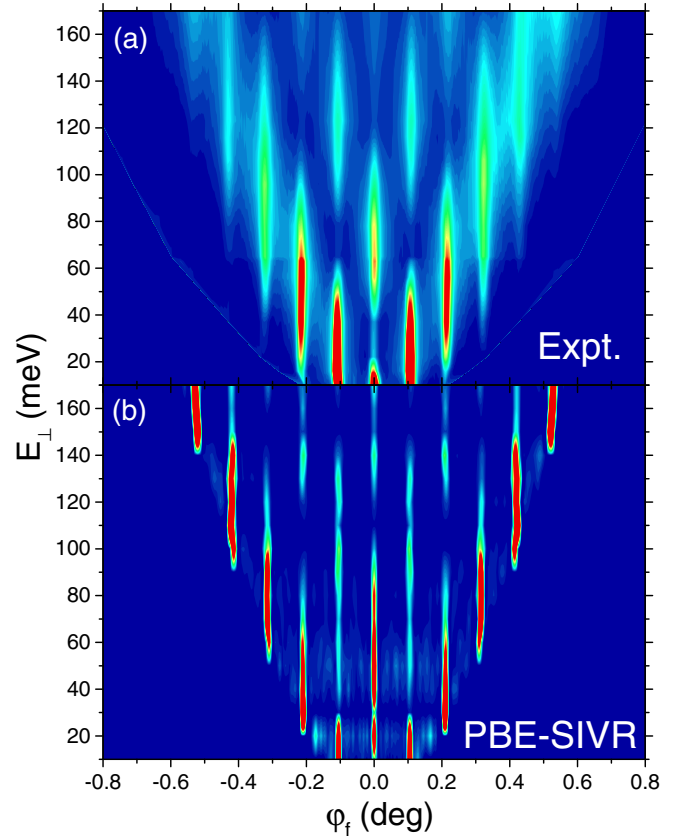


FIG. 2. Two-dimensional diffraction charts, in terms of the normal energy E_{\perp} and the azimuthal angle φ_f for impact energy $E = 600$ eV. (a) Experiment and (b) SIVR simulation with the PBE PES.

equivalent parallel channels, satisfying $\sin \varphi_f = n\lambda/D$ with $\lambda = 2\pi/K_i$, D the channel width and n the Bragg order ($n = 0$ for the in-plane reflection). The intensity modulation (both azimuthal and in normal energy) of the Bragg orders is in contrast ruled by intrachannel interference, a well-known challenge for all GIFAD models [4] due to its extraordinary sensitivity to the potential features and the description of the rainbow region. Intrachannel interference is given by the potential landscape within a single channel, which gives rise to the rainbow and supernumerary rainbows maxima. The intrachannel pattern acts as an envelope function for the Bragg maxima, determining their intensities.

The simulated chart in Fig. 2 fairly reproduces the experimental trend despite some noticeable differences, such as the apparent shift to lower E_{\perp} by about 20 meV in the outermost peaks of the simulated chart (similar to those present in Refs. [9,17]), the high intensity of these peaks at the highest E_{\perp} values, and the azimuthal width of the streaks. These quantitative discrepancies might be the result of processes not contemplated by our model, such as inelastic effects, defects, vdW interaction, etc. Concerning inelastic mechanisms, fingerprints of the physisorption well have been recently explored in polar profiles [38]. Note as well that, given the reported sensitivity of the streaks azimuthal width to the collimation setup [13,39], our simulations were carried out under the same collimation conditions as the experiment.

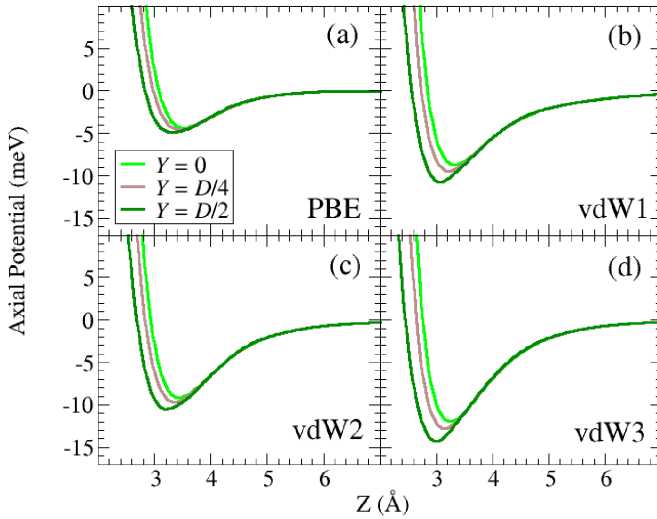


FIG. 3. Axial potential as a function of the He-surface distance Z for fixed values of the coordinate Y across the $\langle 100 \rangle$ channel. Different exchange-correlation functionals are considered in each panel: (a) PBE, (b) vdW1, (c) vdW2, and (d) vdW3 (see text for the labeling of vdW approaches).

B. PES analysis

The He-surface potential V_{PS} is a central ingredient in our GIFAD simulations, which consider its full 3D character. The scattering process in GIFAD, however, is mainly ruled by the axial potential $V^{2D}(Y, Z)$, obtained from averaging V_{PS} along the channeling direction (\hat{x}) [40], with Y the position across the channel and Z the vertical He-surface distance. In Fig. 3, we plot the axial PBE, vdW1, vdW2, and vdW3 potentials as functions of Z . The displayed curves correspond to Y values across the $\langle 100 \rangle$ channel, with $Y = Y_B = 0$ and $Y = Y_M = D/2$, respectively, its border (B) and middle (M) [see Fig. 4]. Note that rows of alternating K^+ and Cl^- ions run along the borders of the $\langle 100 \rangle$ channel, while there are no surface atoms in its middle.

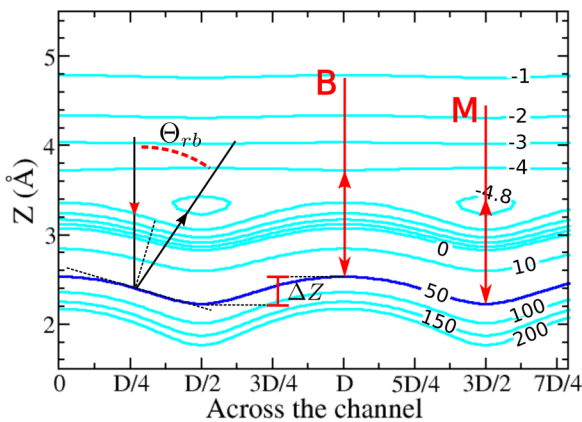


FIG. 4. PBE equipotential curves of the axial potential along $\langle 100 \rangle$ depicting the HCW (intrinsic) corrugation, the rainbow angle and in-plane B and M trajectories for a given E_{\perp} . Normal energy values are in meV. Nonlabeled curves correspond to values -1 , -2 , -3 , and -4 meV.

The salient feature in Fig. 3 is the physisorption well, particularly, its presence in Fig. 3(a). Attractive contributions to the potential are typically assumed to be polarization and/or vdW in nature. However, notwithstanding the no-polarization no-vdW scenario, respectively ensured by the $\langle 100 \rangle$ channel and the PBE potential, Fig. 3(a) exhibits a shallow well, around 5 meV deep in the 3.2–3.5 Å Z range, which provides evidence for an additional attractive contribution, likely exchange-correlation in origin [41]. Regarding dispersion contributions to the axial potential for He-KCl(001), polarization effects have been reported along $\langle 110 \rangle$ [2], while vdW effects are visible in Figs. 3(b)–3(d), when compared to Fig. 3(a). In all cases, vdW dispersion forces result in a deeper well and a larger variation of its location Z with the coordinate Y across the channel.

Physisorption wells can be probed by low normal energy He atoms with high sensitivity through the dynamical effects they induce on GIFAD-related properties such as the surface corrugation and rainbow angle. The processing of an experimental GIFAD pattern [2] yields the shape of an equipotential curve (associated to a given normal energy) from the modulation of the Bragg pattern along the azimuthal angle. The surface corrugation and rainbow angle are then, respectively, derived from the amplitude and maximum slope of this effective potential. Within a hard corrugated wall (HCW) model [42], however, these quantities can be determined, for a given E_{\perp} , from geometric properties of the $V^{2D}(Y, Z) = E_{\perp}$ equipotential curve, as illustrated in Fig. 4 for the $\langle 100 \rangle$ channel and PBE potential. The *intrinsic* corrugation $\Delta Z^{(HCW)}(E_{\perp}) = Z_{\max} - Z_{\min}$ is determined by the Z positions of this curve's maximum (Z_{\max}) and minimum (Z_{\min}), while its maximum slope $\max(dZ/dY)$ gives the angle of maximal deflection, i.e., the rainbow angle $\Theta_{rb}(E_{\perp})$. Note that within this HCW description, the rainbow maximum can also be described in classical terms, resulting from the accumulation of trajectories reflected near an inflection point in $Z(Y)$.

Noteworthy, the HCW (intrinsic) corrugation and rainbow, derived directly from the axial potential (and hence alternatively referred to as PES corrugation and rainbow), cannot provide a complete picture of the scattering process as they do not take into account either the persistence of the He-surface interaction throughout the scattering process or the quantum effects involved in the rainbow scattering. Instead, within the SIVR approach, the surface corrugation is associated with the in-plane intensity, at $\varphi_f = 0$, of the simulated GIFAD pattern, while the rainbow angle is determined by the bright outermost maximum in the intrachannel pattern, which takes into account quantum effects like the dark side of the classical rainbow angle [12,43].

C. Surface corrugation: Dynamical effects and phase analysis

In this section, we will restrict our theoretical analysis to SIVR simulations with the PBE potential to show how dynamical effects contribute to the surface corrugation derived from experimental GIFAD patterns. Then, by means of a detailed monitoring of the evolution of the phase associated with relevant trajectories, we will prove the direct connection between the behavior of the experimental (*effective*) corrugation at low normal energy and the physisorption well.

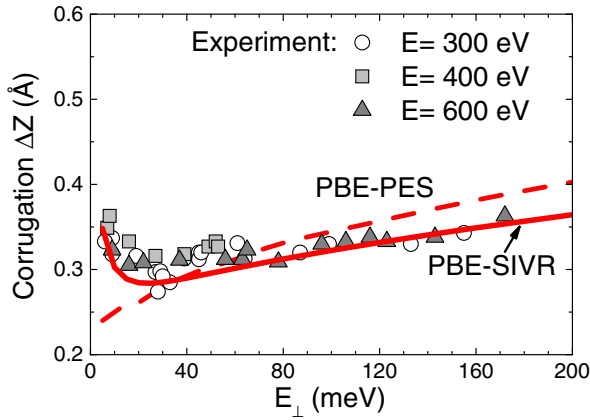


FIG. 5. Surface corrugation as a function of the normal energy E_{\perp} obtained from experimental GIFAD patterns, the PBE PES (HCW value) and SIVR simulations (with the PBE PES), the latter given by Eq. (4).

1. Dynamical contribution to the effective corrugation

The SIVR specular intensity of a GIFAD pattern is determined from the interference between partial transition amplitudes corresponding to trajectories contained in the scattering plane, i.e., impinging along the channel border (B) or middle (M) [see Fig. 4]. The phase difference between B and M trajectories is associated with their respective reflection distances to the surface Z_{\max} and Z_{\min} and, hence, we define the SIVR corrugation in a manner analogous to the HCW one [42], that is,

$$\Delta Z^{(\text{SIVR})} = \frac{\phi_B^{(\text{SIVR})} - \phi_M^{(\text{SIVR})}}{2K_{iz}}, \quad (4)$$

where $\phi_B^{(\text{SIVR})}$ and $\phi_M^{(\text{SIVR})}$ are the respective phases for B and M trajectories, given by Eq. (3) for $t \rightarrow +\infty$, and $K_{iz} = \sqrt{2m_p E_{\perp}}$ is the component of the initial momentum perpendicular to the surface plane. Despite this HCW-like definition, the SIVR corrugation is not proportional to the intrinsic one as B and M trajectories experience different potential landscapes and these *dynamical effects* also contribute to their phase difference. Consequently, the SIVR corrugation contains information of both the intrinsic corrugation and dynamical effects and can then be expressed as

$$\Delta Z^{(\text{SIVR})} = \Delta Z^{(\text{HCW})} + \Delta Z^{(\text{dyn})}. \quad (5)$$

The effective (from experiments), intrinsic (from the PES) and SIVR corrugations for He-KCl(001) have recently been addressed for $\langle 110 \rangle$ incidence [2] and in Fig. 5 we analogously show these quantities as functions of E_{\perp} along $\langle 100 \rangle$. Upon decreasing E_{\perp} , experiments show a slightly decreasing behavior down to 30 meV when the tendency reverts and corrugation starts to increase, though in a less eye-catching fashion than the one obtained for $\langle 110 \rangle$. However, there is more to this behavior than this first-glance impression. The intrinsic corrugation $\Delta Z^{(\text{HCW})}(E_{\perp})$, obtained from the axial PBE PES, monotonically decreases thus failing to capture the low E_{\perp} experimental increase. In contrast, the SIVR corrugation $\Delta Z^{(\text{SIVR})}(E_{\perp})$ is in almost quantitative accord with the experiment in the whole E_{\perp} range considered, which,

combined with Eq. (5), means that dynamical effects are the origin of the increase in the experimental corrugation for $E_{\perp} \lesssim 30$ meV.

A measure of the increasing importance of dynamical effects for low E_{\perp} can be obtained from the relative difference $\Delta Z^{(\text{dyn})}/\Delta Z^{(\text{HCW})}$, which reaches 20% for $E_{\perp} = 10$ meV and 46% for $E_{\perp} = 5$ meV, lower though comparable to the respective 38% and 55% reported for $\langle 110 \rangle$ [2]. When compared with $\langle 110 \rangle$ [2], the corrugation increase for $\langle 100 \rangle$ appears at lower E_{\perp} and is less intense, due to the monotonically decreasing behavior of its intrinsic corrugation. Nevertheless, dynamical effects along $\langle 100 \rangle$ are intense enough to produce the slope inversion of the experimental and SIVR corrugations.

2. Analysis of the SIVR phase

As previously stated, the origin of the observed dynamical effects for low E_{\perp} is related to the physisorption well. Following, we prove this claim through the analysis of SIVR phases $\phi_B^{(\text{SIVR})}$ and $\phi_M^{(\text{SIVR})}$ [see Eq. (4)].

Within a HCW scattering the phase $\phi^{(\text{HCW})}$ is given by

$$\phi_j^{(\text{HCW})}(Z) = \begin{cases} 2K_{iz}(Z_0 - Z) & \text{incoming path} \\ 2K_{iz}(Z_0 - Z_{tp}) & \text{outgoing path,} \end{cases} \quad (6)$$

with Z_{tp} the trajectory's turning point ($Z_{tp}^{(B)} = Z_{\max}$ and $Z_{tp}^{(M)} = Z_{\min}$ for B and M trajectories, respectively), and Z_0 the initial and final He-surface distance, for which V_{PS} is negligible. The difference

$$\phi^{(\text{dyn})} = \phi^{(\text{SIVR})} - \phi^{(\text{HCW})} \quad (7)$$

thus isolates the dynamical contribution to the SIVR phase, which evolves steered by the potential landscape experienced by the projectile along the trajectory [see Eq. (3)]. In Fig. 6, this effect is visualized for B and M trajectories with $E_{\perp} = 10$ meV, whose phases $\phi^{(\text{dyn})}$ are plotted as functions of the He-surface distance Z , together with the respective axial potential curves.

From Fig. 6, the evolution of the phase $\phi^{(\text{dyn})}$ with Z can be directly associated with the features of the potential and, for very low E_{\perp} , this significantly involves the attractive region. For the incoming M trajectory, $\phi^{(\text{dyn})}$ increases from Z_0 down to the position of the well bottom Z_{wb} , together with its first derivative, while the kinetic energy of the normal motion increases. Note that at Z_{wb} there is an inflection point in $\phi^{(\text{dyn})}$. From Z_{wb} to the position of the potential root Z_{we} (well edge), the derivative $\partial\phi^{(\text{dyn})}/\partial Z$ decreases as does the normal kinetic energy and at Z_{we} the phase $\phi^{(\text{dyn})}$ reaches a local maximum. The last incoming interval is from Z_{we} to Z_{tp} , where $\phi^{(\text{dyn})}$ and its derivative decrease as does the normal kinetic energy. In summary, $\partial\phi^{(\text{dyn})}/\partial Z$ follows the normal kinetic energy [Fig. 6(b)] and is proportional to the momentum p_z throughout the incoming part of the M trajectory and an analogous direct connection can be made for its outgoing part, as well as for the complete B trajectory.

As enlightening as Fig. 6 is, it still does not by itself provide the explanation of the experimental corrugation depicted in Fig. 5. The next step in our analysis is then to separate the accumulated phase resulting from the attractive part of the potential, $\Phi_{\text{att}}^{(\text{dyn})}$, from that resulting from the repulsive

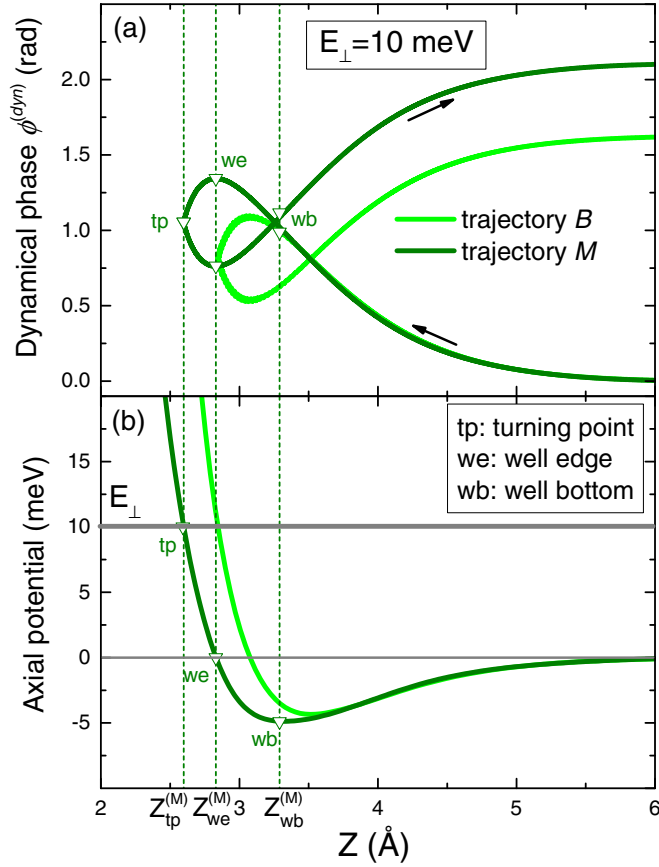


FIG. 6. For border (B) and middle (M) trajectories, with $E_{\perp} = 10$ meV and the PBE potential, we show (a) the phase $\phi^{(\text{dyn})} = \phi^{(\text{SIVR})} - \phi^{(\text{HCW})}$ due to dynamical effects and (b) the axial potential along each trajectory. Both quantities are plotted as functions of Z .

part, $\Phi_{\text{rep}}^{(\text{dyn})}$, associated with the reflection process. Given the symmetry of the problem, we can restrict our analysis to the incoming part of the trajectory. The accumulated phases are then given by

$$\begin{aligned}\Phi_{\text{att}}^{(\text{dyn})} &= \phi^{(\text{dyn})}(Z_{\text{we}}) - \phi^{(\text{dyn})}(Z_0), \\ \Phi_{\text{rep}}^{(\text{dyn})} &= \phi^{(\text{dyn})}(Z_{\text{tp}}) - \phi^{(\text{dyn})}(Z_{\text{we}}),\end{aligned}\quad (8)$$

and they are plotted, as functions of E_{\perp} , for B and M trajectories in Fig. 7. From Fig. 7, we can obtain the difference of the accumulated phase along B and M trajectories for both the attractive and repulsive regions,

$$\begin{aligned}\Delta\Phi_{\text{rep}}^{(\text{dyn})} &= (\Phi_B^{(\text{dyn})} - \Phi_M^{(\text{dyn})})_{\text{rep}}, \\ \Delta\Phi_{\text{att}}^{(\text{dyn})} &= (\Phi_B^{(\text{dyn})} - \Phi_M^{(\text{dyn})})_{\text{att}}.\end{aligned}\quad (9)$$

Then, adding up these contributions we get

$$\Delta\Phi^{(\text{dyn})} = \Delta\Phi_{\text{rep}}^{(\text{dyn})} + \Delta\Phi_{\text{att}}^{(\text{dyn})},\quad (10)$$

and, through Eq. (4), the phase difference $2\Delta\Phi^{(\text{dyn})}$ (the factor of 2 is required to include the outgoing part of the trajectory) provides the dynamical contribution to the corrugation. It is clear in Fig. 7 that $\Delta\Phi_{\text{rep}}^{(\text{dyn})}$ becomes negligible in the low E_{\perp} limit. Thus it is $\Delta\Phi_{\text{att}}^{(\text{dyn})}$ that determines the low E_{\perp} behavior of the SIVR and experimental corrugations displayed

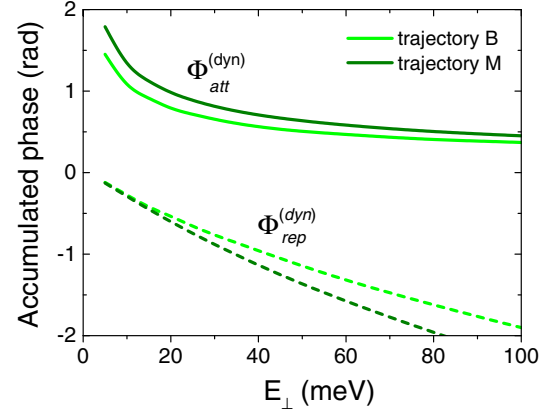


FIG. 7. Accumulated phase $\Phi^{(\text{dyn})}$ for border (B) and middle (M) trajectories (incoming path) as functions of E_{\perp} . Solid and dashed lines, respectively, correspond to $\Phi^{(\text{dyn})}$ evaluated in the attractive and the repulsive regions.

in Fig. 5. This proves that the experimental corrugation increase for low E_{\perp} results from dynamical effects due to the physisorption well. What is more, a similar analysis easily extends the validity of the result to the $\langle 110 \rangle$ channel.

At this point, it is worth noting that the role of the physisorption well as the dominant source of dynamical effects is restricted to the low E_{\perp} region, $E_{\perp} \lesssim 30$ meV. For higher normal energies, the repulsive region of the axial potential provides the dominant dynamical contribution to $\Delta\Phi^{(\text{dyn})}$ as straightforwardly deduced from Fig. 7.

D. Dynamical contribution to the rainbow angle

Within the SIVR approximation, the rainbow peak is the intense outermost maximum in the intrachannel contribution to a GIFAD pattern. In this section, we will address how SIVR trajectories differ from HCW paths regarding the predicted location of the rainbow peak. As in the previous section, we restrict our analysis to SIVR simulations with the PBE potential.

The surface corrugation and the rainbow angle complement each other as the former probes the flatter regions of the potential landscape, while the latter examines the steepest ones. Another relevant difference is that SIVR trajectories contributing to the rainbow peak inspect a much more extended area across the channel than their corrugation counterparts (B and M trajectories which run along the channel), making the rainbow angle much more sentient to dynamical effects and changes in the potential.

In Fig. 8, we show the rainbow angle Θ_{rb} obtained from the processing of experimental GIFAD patterns as a function of E_{\perp} , contrasting it with the HCW rainbow $\Theta_{rb}^{(\text{HCW})}$, geometrically obtained from the potential [see Fig. 4], and the SIVR rainbow, $\Theta_{rb}^{(\text{SIVR})}$, evaluated from simulated pure intrachannel patterns.

The experimental rainbow angle in Fig. 8 is approximately constant for $E_{\perp} > 60$ meV and slowly increasing for lower E_{\perp} . In this latter region the data spread a little, and this spreading is larger than the one obtained for the corrugation due to the larger uncertainty involved in the evaluation of a

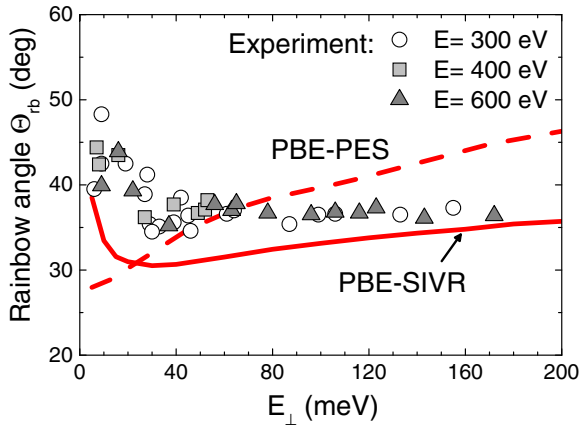


FIG. 8. Rainbow angle as a function of E_{\perp} . Symbols and lines analogous to Fig. 5.

second derivative (the maximum slope). The rainbow angle $\Theta_{rb}^{(HCW)}$ obtained from the potential (PBE PES) corresponds to an unrealistic HCW dynamics and yields, for decreasing E_{\perp} , a monotonic decreasing behavior in poor accord with the experiment. Instead, $\Theta_{rb}^{(SIVR)}$ obtained from simulated intrachannel patterns greatly improves the agreement with the experimental data as they both include dynamical effects.

As was the case for the corrugation, dynamical effects for low E_{\perp} can be traced to the presence of the physisorption well. This is clearly visualized in Fig. 9 where, in the top panel [Fig. 9(a)], a selection of trajectories contributing to the rainbow peak is plotted within an equipotential map, while the bottom panel [Fig. 9(b)] depicts the corresponding axial potential curves. Any of these trajectories $z_t(y_t)$ can be split into three sections—incoming, reflection, and outgoing—where the potential $V^{2D}(y_t, z_t)$ is, respectively, attractive, repulsive, and attractive again. Note that in the latter region, the

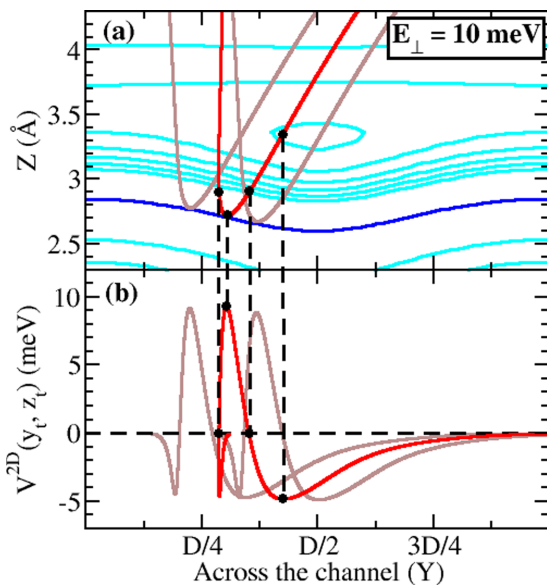


FIG. 9. (a) SIVR trajectories deflected to $\Theta_f \sim \Theta_{rb}$, with $E_{\perp} = 10$ meV and the PBE potential. (b) Axial potential along each of the depicted rainbow trajectories $z_t(y_t)$.

trajectory's inflection point, determined from the maximum of dz_t/dy_t , occurs at (Y, Z) coordinates which give the minimum potential along the trajectory. Another feature worth mentioning is that the maxima of the potentials along the selected trajectories are slightly below 10 meV because trajectories transfer a little momentum to the direction across the channel ($p_z \rightarrow p_y$) before reaching their turning points, where $p_z = 0$.

At this point, we will return to Fig. 8 where it is evident that for the $\langle 100 \rangle$ channel, dynamical effects are not limited to the low E_{\perp} region but rather they are clearly visible in the whole normal energy range considered. However, for $E_{\perp} \gtrsim 100$ meV, rainbow trajectories are not altered by the shallow attractive potential and dynamical effects take place in the reflection region due to the repulsive potential. We can then conclude that the relevance of the attractive and repulsive regions depends on the E_{\perp} value, this being observed both for the corrugation and the rainbow angle through the respective analysis of the SIVR phase and the rainbow trajectories.

E. The role of van der Waals interactions

Heretofore, our theoretical analysis of the surface corrugation and rainbow angle has been made with a PBE potential, which disregards interactions between induced dipoles, i.e., vdW interactions. This level of approximation yielded excellent agreement with experiment for the $\langle 110 \rangle$ channel [2] and it also performed very well for the corrugation along $\langle 100 \rangle$, as shown in Fig. 5. However, the SIVR-Experiment accord for the rainbow angle depicted in Fig. 8 was not as rewarding. This discrepancy could be associated with the higher sensitivity of the rainbow angle to details of the potential, in particular the neglect of vdW interactions, which markedly affect the physisorption well, as shown in Fig. 3. Therefore, in this section we will study the role of vdW interactions on the corrugation and rainbow angle for the $\langle 100 \rangle$ channel.

Motivated by the unsatisfactory description of low electron-density regions provided by local and semilocal exchange-correlation functionals, several approaches have been developed to incorporate vdW interactions within DFT [31–33,44–49]. In this paper, we compare the performance of three of them, already introduced in Secs. III B and IV B. Note that while both vdW1 and vdW2 incorporate vdW interactions in a self-consistent fashion and may additionally alter (i.e., improve) the PBE functional in regions where vdW contributions are negligible, vdW3 was the method used in early GIFAD and rainbow scattering studies of He-KCl(001) [14], which introduces a semiempirical correction at large distances, is not self-consistent and is matched to the PBE potential at small distances.

The intrinsic (PES) and SIVR corrugations obtained with vdW1, vdW2, and vdW3 potentials are displayed in Fig. 10 together with the effective corrugation derived from experiments. The reference PBE-PES and PBE-SIVR curves are included as well. The qualitative behavior of the SIVR and intrinsic corrugations is not altered upon switching from PBE to the vdW PESs. When compared to the PBE SIVR corrugation, vdW1 and vdW3 yield a poorer agreement with experiment. In contrast, vdW2 satisfactorily matches the experimental values which, for very low E_{\perp} fall between the PBE and vdW2 curves, suggesting this latter vdW functional gives an

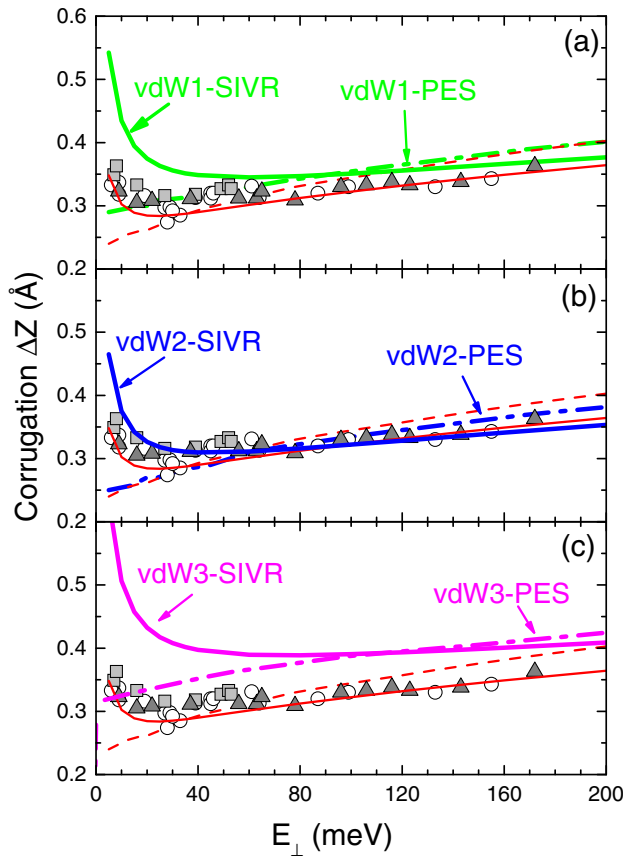


FIG. 10. Corrugation as a function of E_{\perp} . Symbols and color lines analogous to Fig. 5 with (a) vdW1, (b) vdW2, and (c) vdW3 potentials. In all panels, red thin lines correspond to PBE-SIVR i (solid) and PBE-PES (dashed) results, and are meant to be used as a reference.

appropriate representation of the flat regions in the potential. However, the comparison of the corrugations obtained with PBE-SIVR and vdW-SIVR allow for no strong claims regarding the role of vdW in GIFAD for $\text{He} \rightarrow \langle 100 \rangle \text{KCl}(001)$.

In fact, the rainbow angle is, as previously mentioned, a more interesting physical quantity for addressing vdW effects and, in Fig. 11, experimental, PBE-SIVR, and vdWs-SIVR rainbow angles are displayed together with the HCW values taken from the respective potentials. From a first inspection, it is clear that vdW3 does not provide a good description of the rainbow angle, so we will focus our discussion on vdW1 and vdW2 approaches. The HCW rainbows obtained from vdW1 and vdW2 are very similar to the PBE reference, in poor accord with the experimental data. This is to be expected as a single equipotential curve determines the rainbow angle for each E_{\perp} and therefore the effect of the physisorption well is mostly neglected. In contrast, the SIVR rainbow angle for a single E_{\perp} carries information of the potential throughout the rainbow scattering trajectories, resulting in a much higher sensitivity. Remarkably, both vdW1-SIVR and vdW2-SIVR improve the accord with experiment, particularly so for $E_{\perp} < 80$ meV. What is more, vdW1 quantitatively reproduces the experimental rainbow for the whole normal energy range considered.

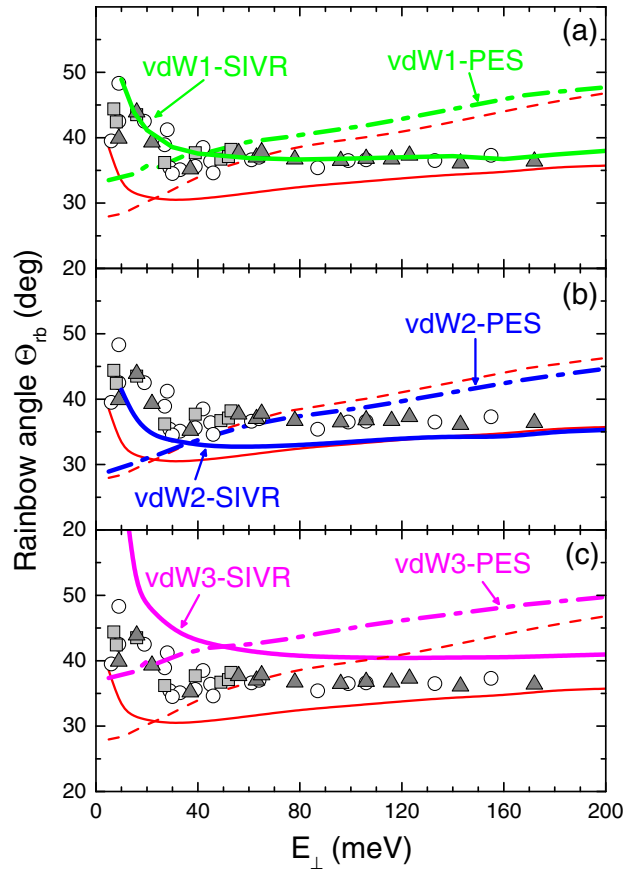


FIG. 11. Rainbow deflection angle as a function of E_{\perp} . Symbols and lines analogous to Fig. 10.

Combining the information obtained from Figs. 10 and 11 we can say that both vdW1 and vdW2 provide a satisfactory description of the interaction potential. vdW1 gives a very good performance for the rainbow, i.e., better describes the highest-slope regions of the potential landscape, while vdW2, though not as good as the vdW1 rainbow description, provides a more general improvement over the PBE potential, involving both flat and high-slope regions.

V. CONCLUSIONS

In this paper, we have addressed fast He diffraction from $\text{KCl}(001)$ for grazing incidence conditions along the $\langle 100 \rangle$ channel. Our study has focused on the physisorption well showing that, for low E_{\perp} , it is a source of dynamical effects which deviate the surface corrugation and rainbow angle from the HCW predictions, producing an increase of both quantities. This connection is accomplished through respective thorough analysis of (a) the SIVR phase associated to in-plane scattering and (b) rainbow trajectories.

Upon inclusion of vdW interactions, the resulting slight changes, of just a few meV, on the physisorption region translate into alterations of the surface corrugation and rainbow angle, the latter being particularly significant. Therefore, the present paper achieves a robust description of the hitherto elusive vdW effects on GIFAD-related physical quantities, thus positioning GIFAD and the SIVR method in the map

of sensitive quality checks for different approaches aimed to describe vdW interactions within DFT [50].

Additional points worth mentioning are (a) theoretical and experimental results are obtained independently, (b) the physisorption well persists even in a no-polarization no-vdW scenario, such as that provided by the $\langle 100 \rangle$ incidence and the PBE potential and, (c) for the $\langle 100 \rangle$ channel, dynamical effects are not restricted to the low E_{\perp} region. For higher normal energies, $E_{\perp} \gtrsim 60$ meV, the repulsive potential is a relevant source of dynamical effects, while the role of the physisorption well becomes negligible.

As future perspectives, the analysis tools developed in this paper for He-KCl(001) could be applied to other alkali-halide surfaces and/or noble gas atoms to check if vdW interactions are also relevant for those systems and compare the performance of the different approaches.

ACKNOWLEDGMENTS

The authors acknowledge funding from ANPCYT (No. PICT-2017-1201 and No. PICT-2017-2945), CONICET (No. PIP 112 201301 00386 CO and No. PIP 112 201501 00274 CO), and U.N. Cuyo (No. 06/C590).

-
- [1] G. Vidali, G. Ihm, H. Y. Kim, and M. W. Cole, *Surf. Sci. Rep.* **12**, 135 (1991).
- [2] G. A. Bocan, H. Breiss, S. Szilasi, A. Momeni, E. M. Staicu Casagrande, M. S. Gravielle, E. A. Sánchez, and H. Khemliche, *Phys. Rev. Lett.* **125**, 096101 (2020).
- [3] M. Debiossac, A. Zugarramurdi, P. Lunca-Popa, A. Momeni, H. Khemliche, A. G. Borisov, and P. Roncin, *Phys. Rev. Lett.* **112**, 023203 (2014).
- [4] M. Debiossac, P. Roncin, and A. G. Borisov, *J. Phys. Chem. Lett.* **11**, 4564 (2020).
- [5] M. S. Gravielle and J. E. Miraglia, *Phys. Rev. A* **78**, 022901 (2008).
- [6] J. P. Perdew, K. Burke, and M. Ernzerhof, *Phys. Rev. Lett.* **77**, 3865 (1996).
- [7] A. Schüller, D. Blauth, J. Seifert, M. Busch, H. Winter, K. Gärtner, R. Włodarczyk, J. Sauer, and M. Sierka, *Surf. Sci.* **606**, 161 (2012).
- [8] M. Debiossac, A. Zugarramurdi, H. Khemliche, P. Roncin, A. G. Borisov, A. Momeni, P. Atkinson, M. Eddrief, F. Finocchi, and V. H. Etgens, *Phys. Rev. B* **90**, 155308 (2014).
- [9] M. del Cueto, A. S. Muzas, F. Martín, and C. Díaz, *Nucl. Instrum. Methods Phys. Res., Sec. B* **476**, 1 (2020).
- [10] G. A. Bocan, J. D. Fuhr, and M. S. Gravielle, *Phys. Rev. A* **94**, 022711 (2016).
- [11] M. S. Gravielle, J. E. Miraglia, and G. A. Bocan, in *State-of-the-Art Reviews on Energetic Ion-Atom and Ion-Molecule Collisions*, Interdisciplinary Research on Particle Collisions and Quantitative Spectroscopy Vol. 2 (World Scientific, Singapore, 2019), Chap. 7, pp. 177–203.
- [12] M. S. Gravielle and J. E. Miraglia, *Phys. Rev. A* **90**, 052718 (2014).
- [13] M. S. Gravielle and J. E. Miraglia, *Phys. Rev. A* **92**, 062709 (2015).
- [14] U. Specht, M. Busch, J. Seifert, H. Winter, K. Gärtner, R. Włodarczyk, M. Sierka, and J. Sauer, *Nucl. Instrum. Methods Phys. Res. Sec. B* **269**, 799 (2011).
- [15] U. Specht, M. Busch, J. Seifert, A. Schüller, H. Winter, K. Gärtner, R. Włodarczyk, M. Sierka, and J. Sauer, *Phys. Rev. B* **84**, 125440 (2011).
- [16] E. Meyer, Habilitationsschrift, Ph.D. dissertation, Humboldt Universität Berlin, Germany, 2015, <http://dx.doi.org/10.18452/17442>.
- [17] G. A. Bocan and M. S. Gravielle, *Nucl. Instrum. Methods Phys. Res. Sec. B* **421**, 1 (2018).
- [18] A. Momeni, E. M. Staicu Casagrande, A. Dechaux, and H. Khemliche, *J. Phys. Chem. Lett.* **9**, 908 (2018).
- [19] H. Khemliche, P. Rousseau, P. Roncin, V. H. Etgens, and F. Finocchi, *Appl. Phys. Lett.* **95**, 151901 (2009).
- [20] W. H. Miller, *J. Chem. Phys. A* **105**, 2942 (2001), and references therein.
- [21] J. H. Van Vleck, *Proc. Natl. Acad. Sci. USA* **14**, 178 (1928).
- [22] W. H. Miller, *J. Chem. Phys.* **53**, 3578 (1970).
- [23] X. Sun and W. H. Miller, *J. Chem. Phys.* **106**, 916 (1997).
- [24] X. Sun and W. H. Miller, *J. Chem. Phys.* **106**, 6346 (1997).
- [25] X. Sun and W. H. Miller, *J. Chem. Phys.* **108**, 8870 (1998).
- [26] D. E. Skinner and W. H. Miller, *Chem. Phys. Lett.* **300**, 20 (1999).
- [27] C. H. Dasso, M. I. Gallardo, and M. Saraceno, *Phys. Rev. C* **75**, 054611 (2007).
- [28] D. P. Dewangan and J. Eichler, *Phys. Rep.* **247**, 59 (1994).
- [29] P. Giannozzi, S. Baroni, N. Bonini, M. Calandra, R. Car, C. Cavazzoni, D. Ceresoli, G. L. Chiarotti, M. Cococcioni, I. Dabo *et al.*, *J. Phys.: Condens. Matter* **21**, 395502 (2009).
- [30] H. F. Busnengo, A. Salin, and W. Dong, *J. Chem. Phys.* **112**, 7641 (2000).
- [31] R. Sabatini, T. Gorni, and S. de Gironcoli, *Phys. Rev. B* **87**, 041108(R) (2013).
- [32] I. Hamada, *Phys. Rev. B* **89**, 121103(R) (2014).
- [33] S. Grimme, *J. Comput. Chem.* **27**, 1787 (2006).
- [34] See Supplemental Material at <http://link.aps.org/supplemental/10.1103/PhysRevB.104.235401> for vdW PESs information.
- [35] N. Ananth, C. Venkataraman, and W. H. Miller, *J. Chem. Phys.* **127**, 084114 (2007).
- [36] R. Gelabert, X. Giménez, M. Thoss, H. Wang, and W. H. Miller, *J. Chem. Phys.* **114**, 2572 (2001).
- [37] W. H. Miller, *J. Phys. Chem. A* **113**, 1405 (2009).
- [38] P. Pan, M. Debiossac, and P. Roncin, *Phys. Rev. B* **104**, 165415 (2021).
- [39] J. Seifert, J. Lienemann, A. Schüller, and H. Winter, *Nucl. Instrum. Methods Phys. Res. Sec. B* **350**, 99 (2015).
- [40] A. Zugarramurdi and A. G. Borisov, *Phys. Rev. A* **86**, 062903 (2012).
- [41] J. E. Miraglia and M. S. Gravielle, *Phys. Rev. A* **95**, 022710 (2017).
- [42] U. Garibaldi, A. C. Levil, R. Spadacini, and G. E. Tommei, *Surf. Sci.* **48**, 649 (1975).

- [43] S. Miret-Artés and E. Pollak, *Surf. Sci. Rep.* **67**, 161 (2012), and references therein.
- [44] M. Dion, H. Rydberg, E. Schröder, D. C. Langreth, and B. I. Lundqvist, *Phys. Rev. Lett.* **92**, 246401 (2004).
- [45] T. Thonhauser, V. R. Cooper, Sh. Li, A. Puzder, P. Hyldgaard, and D. C. Langreth, *Phys. Rev. B* **76**, 125112 (2007).
- [46] A. D. Becke and E. R. Johnson, *J. Chem. Phys.* **127**, 154108 (2007).
- [47] A. Tkatchenko and M. Scheffler, *Phys. Rev. Lett.* **102**, 073005 (2009).
- [48] S. Grimme, J. Antony, S. Ehrlich, and H. Krieg, *J. Chem. Phys.* **132**, 154104 (2010).
- [49] A. Otero de la Roza and E. R. Johnson, *J. Chem. Phys.* **136**, 174109 (2012).
- [50] M. del Cueto, R. J. Maurer, A. Al Taleb, D. Farías, F. Martín, and C. Díaz, *J. Phys.: Condens. Matter* **31**, 135901 (2019).